

## Low-energy irradiation induced giant quasilinear superelasticity over wide temperature range in NiTi shape memory alloys

Chuanxin Liang,<sup>1</sup> Wenbo Liu,<sup>1,3</sup> Hengfeng Gong,<sup>2,\*</sup> and Dong Wang<sup>1,†</sup>

<sup>1</sup>*Center of Microstructure Science, Frontier Institute of Science and Technology,  
State Key Laboratory for Mechanical Behavior of Materials,  
Xi'an Jiaotong University, Xi'an 710049, People's Republic of China*

<sup>2</sup>*Nuclear Fuel and Materials Department, China Nuclear Power Technology Research Institute Co., Ltd,  
Shenzhen 518000, People's Republic of China*

<sup>3</sup>*Department of Nuclear Science and Technology, Xi'an Jiaotong University, Xi'an 710049, People's Republic of China*



(Received 27 November 2021; revised 7 March 2022; accepted 29 March 2022; published 14 April 2022)

Continuous strain glass transition (STGT) in shape memory alloys (SMAs) has attracted much attention and shows potential applications in biomedical, robotics, and micro-electromechanical systems due to its quasilinear superelasticity (SE). However, the reported strain glass system in NiTi alloys through doping antisite point defects can only produce local *R*-phase martensitic domains and show small recoverable strain ( $\sim 1\%$ ), which limits its wide applications. Here, we propose a method to design B19' strain glass with large recoverable strain in NiTi binary alloys by introducing interstitial atoms and vacancies through low-energy irradiation by integrating molecular dynamics and phase field modeling. The interstitial atoms play the most important role to transform the normal martensitic transformation (MT) to STGT. A complete phase diagram is established to describe the relationship between MT/STGT and irradiation energy. The system after large irradiation energy ( $\sim 5.3 \times 10^{12}$  keV/cm<sup>2</sup>) has shown obvious frequency dependence of storage modulus, continuous volume fraction change, and B19' martensitic nanodomains, which confirm the existence of B19' STGT. This B19' strain glass has shown large recoverable strain ( $\sim 5.8\%$ ) over a wide temperature range (from 100 to 300 K), which can be attributed to the continuous nucleation and growth of martensitic nanodomains in this temperature range. Our calculations theoretically proposed a method to design strain glass systems with giant quasilinear SE by interstitial defects and may stimulate the application of SMAs.

DOI: [10.1103/PhysRevMaterials.6.045602](https://doi.org/10.1103/PhysRevMaterials.6.045602)

### I. INTRODUCTION

Shape memory alloys (SMAs) have attracted much attention because of thermoelastic martensitic transformation (MT) [1] induced superelasticity (SE) and shape memory effect (SME), which have been widely used in different fields, e.g., aerospace technology, robotic technology, and micro-electromechanical systems [2,3]. However, the narrow temperature operation window ( $\sim 75$  K after heat treatment) and large hysteresis ( $\sim 250$  MPa) [4] for SE due to the first-order transition characteristic of MT limit its applications in extreme environments and accuracy control. It is well known that there exists a critical point in the axial stress–temperature phase diagram of MT by introducing high temperature and high pressure at which the MT presents a continuous transition behavior and zero hysteresis [5,6]. Interestingly, the recently discovered strain glass transition (STGT) has also shown continuous transition behavior with small hysteresis by introducing sufficient point defects [7–9], which may also be a critical behavior in MT systems. STGT has shown a continuous transition from a dynamically disordered lattice strain state to a frozen dis-

ordered lattice strain state instead of the long-range ordered lattice strain structure [10]. This transition behavior caused by STGT can be attributed to the randomly distributed local stress field caused by doped defects [11], which change the local transition behavior and influence the macroscopic phenomenon.

The continuous STGT has been reported when the defect density (concentration) reaches a certain critical value [7,12,13]. However, only those MT systems with small stress-free transformation strain (SFTS; e.g., *R* phase) have been reported to show continuous STGT in most NiTi SMAs [8,14,15]. According to the theoretical calculations, the formation of continuous STGT with larger SFTS, e.g., B19/B19' strain glass in NiTi SMAs requires stronger local misfit caused by defects [16], and experimental works have confirmed that high-density dislocations could induce B19' STGT [12]. As an important defect, interstitial atoms would occupy the nonequilibrium position of the lattice [17] and produce a large lattice misfit [1], which could be effective to design strain glass with large recoverable strain. However, conventional heat treatment by thermal fluctuation with low energy would only introduce small interstitial atoms with low density, e.g., H ( $\leq 0.027$ ) [18] or cause carbides and/or oxides (e.g., TiC and Ti<sub>4</sub>Ni<sub>2</sub>O<sub>x</sub>) by reacting with O, C, and Si [19,20], which could not result in STGT.

\*gonghengfeng@cgnpc.com.cn

†wang\_dong1223@xjtu.edu.cn

Experimental works have shown that irradiation could cause complex defects (e.g., vacancies, interstitial atoms, precipitates, and dislocation) and significantly change the MT behavior and related properties [21–24]. Lagrange *et al.* [22] observed a nano B19' crystalline structure in amorphous matrix due to a combination of cascade overlapping and damage accumulation after Ni ion irradiation in NiTi SMAs. Wang *et al.* [23] reported the element redistribution and the formation of a multilayer structure consisting of a columnarlike TiH<sub>2</sub> phase, a transition layer Ti<sub>2</sub>Ni phase, and the austenite phase in proton irradiated TiNi alloy. Zhao *et al.* [21] reported the existence of an amorphous phase, TiH<sub>2</sub> and Ti<sub>2</sub>Ni phases in proton irradiated TiNi thin film, and a consequent deterioration of the shape recovery property. Wang *et al.* [24] reported the decrease of the *R*-phase transformation start temperature  $R_s$  and the reverse martensitic transition finish temperature  $A_f$  in proton irradiated TiNi. However, the defect type, distribution, and their influence on the MT behavior caused by irradiation are still unclear. Due to the relatively high cost of irradiation experiments, simulations are widely used to study the effect of irradiation, e.g., molecular dynamics (MD) simulation is always used to simulate the damages at nanoscale (vacancies, interstitial atoms, etc.) [25], and phase field modeling is always used to simulate the damages at microscale (voids, bubbles, etc.) [26]. Simulations to study the effect of irradiation on MT on both atomic and microscopic scale are lacking.

In this paper, a multiscale method integrating MD, molecular statics with a localization function, and phase field modeling are proposed to capture the physical origin of irradiation on MT in NiTi SMAs. MD calculations exhibit that the defect density of the interstitial atom, the vacancy, and the antisite caused by the irradiation increase with the increase of the irradiation fluence and the energy of primary knock-on atom (PKA). It is found that, with the increase of interstitial defect density caused by the increase of irradiation fluence and the energy of PKA, the B19' MT changes from typical first order to continuous B19' STGT. Such B19' STGT has shown SE (~5.8%) with slim hysteresis over a wide temperature range (~200 K). A phase transition diagram of B19' MT and STGT has been established, which exhibits the existence of critical phase transition boundaries which provides quantitative guidance to design critical SMAs with properties.

## II. METHODS

MD simulations are carried out using the classical parallel MD package LAMMPS [27] with the embedded-atom-method interatomic potential [28]. The simulation boxes with three-dimensional periodic boundary conditions are employed to calculate the displacement cascades. The cascade is introduced by setting a PKA which is defined as the first displaced atom during irradiation. The PKA can induce the subsequent lattice site displacements if it possesses sufficient energy or come to rest in the lattice at an interstitial site. In the beginning, the perfect crystal B2 NiTi structure is created and relaxed at 300 K for 15 ps with a time step 1 fs using an isobaric-isothermal ensemble (NPT). Then the first PKA with a recoil energy (2–20 keV) is chosen randomly and given a velocity with random direction  $v = \sqrt{2E_{\text{PKA}}/m}$ , where  $E_{\text{PKA}}$

is the energy of PKA, and  $m$  is the atomic mass. Once the cascade is introduced, the system will run for 75 ps with a canonical ensemble (NVT) followed by quenching to 0 K with energy minimization using the conjugated gradient algorithm. Then the system is re-equilibrated at 300 K, and the first cascade is finished. The subsequent cascades are introduced one by one using the same approach. The Wigner-Seitz cell method is implemented to analyze the point defects, i.e., vacancies, interstitial atoms, and antisite defects. To avoid the size effect in MD, we introduce 40 PKAs with the recoil energy 20 keV to the simulation boxes with different sizes  $l \times l \times l a_0^3$  ( $a_0$  is the lattice constant and  $l = 30, 40, 50, 55, 60, \text{ and } 70$ ), and the calculated number of interstitial atoms and antisite defects are shown in Fig. 1. When the  $l$  is  $< 50$ , the number of interstitial atoms and antisite defects shows large fluctuations; however, when the  $l$  is  $\geq 55$ , the number of interstitial atoms and antisite defects shows steady increase and small fluctuations with the increase of the number of PKAs. To keep computational efficiency and convergence, the simulation box size is set to  $55 \times 55 \times 55 a_0^3$  (332 750 atoms) in the following simulations. It should be noted that, for convenience, we assume that the whole simulation box is at the same depth from the surface, and we used periodic boundary condition and ignored the angle of incidence of the irradiation particles which is reasonable because the length of the side of the simulation box is small (~16.5 nm) compared with the irradiation depth ( $> 1000$  nm).

The atomic stress on atom  $i$  is described with the virial stress [29–31] at the ground state:

$$W_i^{ab} = \frac{1}{\Omega} \left( -\frac{1}{2} \sum_{j \neq i} f_{ij}^a r_{ij}^b + \dots \right), \quad (1)$$

where  $\Omega$  is the atomic volume,  $r_{ij}^b$  is the  $b$  component of the vector from atom  $i$  to atom  $j$ , and  $f_{ij}^a$  is the  $a$  component of the force on atom  $i$  exerted by atom  $j$  in which  $a, b = 1, 2, 3$  indicates the directions. The ellipsis represents that there may be higher-order atomic virial stress contributions according to the interatomic potentials used in the simulation.

The continuum stress field is calculated by utilizing an enforced stoichiometry and atomic localization function approach [32] to the atomic stress field  $W_i^{ab}$ :

$$\Pi^{ab}(\mathbf{r}) = \sum_X \phi_X(\mathbf{r}) \sum_{i \in X} P(\mathbf{r} - \langle \mathbf{r}_i \rangle) W_i^{ab}, \quad (2)$$

where the localization function  $P(\mathbf{r})$  is used to smear out the contribution of an individual atom to the whole system, and the stoichiometric function  $\phi_X(\mathbf{r})$  is used to achieve the correct stoichiometry in multicomponent systems when the resolution of the stress field is high. Here,

$$P(\mathbf{r}) = \frac{27}{\alpha^3 (2\pi)^{3/2}} \exp\left(-\frac{9r^2}{2\alpha^2}\right), \quad (3)$$

$$\phi_X(\mathbf{r}) = \frac{\sum_j P(\mathbf{r} - \langle \mathbf{r}_j \rangle)}{\sum_{j \in X} P(\mathbf{r} - \langle \mathbf{r}_j \rangle)} \frac{n_X}{\sum_Y n_Y}, \quad (4)$$

where  $\alpha$  is equivalent to a triple standard deviation and determines the shape of the function. Here,  $X$  denotes the element type, and  $n_X$  is the number of atom  $X$ . The choice of  $\alpha$  is 5 Å based on our previous calculation [11]. The details of the

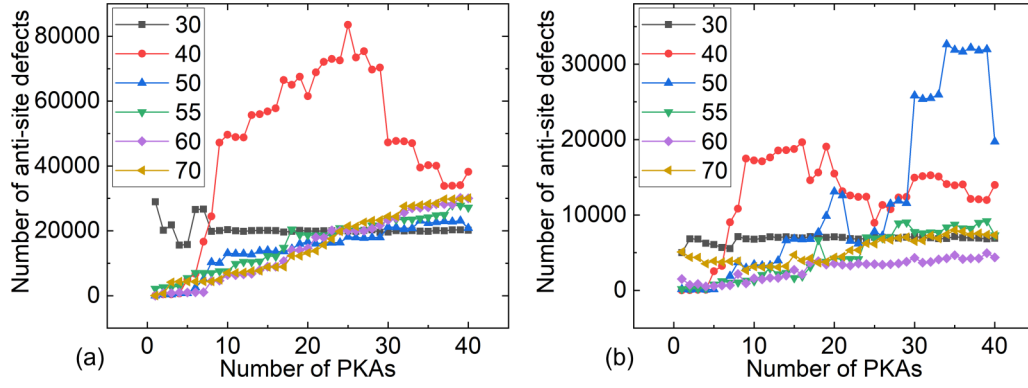


FIG. 1. (a) and (b) The number of interstitial atoms and antisite defects vs the number of primary knock-on atoms (PKAs; 20 keV) in the molecular dynamics (MD) simulation boxes of different sizes  $l \times l \times l a_0^3$  ( $l = 30, 40, 50, 55, 60,$  and  $70$ ).

calculation of continuum stress field from atomic stress can be found in our previous work [11] and Ref. [32].

An MT from B2 to B19' (12 variants) is considered in our phase field modeling with the SFTS tensors  $\varepsilon_{ij}^p$  ( $p = 1-12$ ) according to lattice correspondence [33]. The total free energy of the system contains chemical free energy, elastic interaction energy caused by the local stress field, gradient interfacial energy, elastic strain energy caused by the formed martensitic domains, and elastic energy caused by applied stress described as follows:

$$F = \int d^3\mathbf{r}(f_{ch} + f_L + f_{gr}) + E_{el} + E_{\text{applied}}. \quad (5)$$

The local chemical free energy is approximated by a Landau expansion polynomial:

$$f_{ch} = \frac{1}{2}A_1 \sum_{i=1-12} \eta_i^2(\mathbf{r}) - \frac{1}{4}A_2 \sum_{i=1-12} \eta_i^4(\mathbf{r}) + \frac{1}{6}A_3 \left[ \sum_{i=1-12} \eta_i^2(\mathbf{r}) \right]^3, \quad (6)$$

where  $\eta_p$  ( $p = 1-12$ ) is the structure order (SO) parameter, representing the correspondence variants of the B19' martensitic phase, where  $A_1 = A_1^0(T - T^0)$ , and  $A_2$  and  $A_3$  are constants.

The elastic interaction energy caused by the local stress field is

$$f_L(\mathbf{r}) = - \sum_{p=1-12} \sum_{i,j=1,2,3} \prod_{ij}(\mathbf{r}) \varepsilon_{ij}^p \eta_p^2(\mathbf{r}), \quad (7)$$

and the gradient interfacial energy is described by

$$f_{gr} = \frac{1}{2}\beta \left[ \sum_{i=1-12} (\nabla \eta_i)^2 \right], \quad (8)$$

which is associated with spatial nonuniformities in the SO parameters at interfaces between the B2 and B19' phases and among different variants of the B19' phase [34], where  $\beta$  is the gradient energy coefficient. The fourth term in Eq. (5),  $E_{el}$ , is

the elastic strain energy associated with the MT [35,36]:

$$E_{el} = \frac{1}{2} C_{ijkl} \sum_p \sum_q \varepsilon_{ij}^p \varepsilon_{kl}^q \int \eta_p^2(\mathbf{r}) \eta_q^2(\mathbf{r}) d^3r - \frac{1}{2} \sum_p \sum_q \int \frac{d^3k}{(2\pi)^3} B_{pq}(\vec{n}) \{ \eta_p^2(\mathbf{r}) \}_k \{ \eta_q^2(\mathbf{r}) \}_k^*, \quad (9)$$

where  $C_{ijkl}$  is the elastic modulus,  $\vec{n} = \vec{k}/k$ ,  $\vec{k}$  is the wave vector in the reciprocal space,  $\{ \dots \}_k$  and  $\{ \dots \}_k^*$  are the Fourier transform and its complex conjugate, and  $B_{pq}(\vec{n}) = n_i \sigma_{ij}^p \Omega(\vec{n})_{jk} \sigma_{kl}^q n_l$ , where  $\sigma_{ij}^p = C_{ijkl} \varepsilon_{kl}^p$ , and  $\Omega(\vec{n})_{ij}^{-1} = C_{ijkl} n_k n_l$ .

The last term  $E_{\text{applied}} = - \int \sigma_{ij}^{\text{applied}} \sum_{p=1-12} \varepsilon_{ij}^p \eta_p^2(r) d^3r$  is the elastic energy caused by applied stress  $\sigma_{ij}^{\text{applied}}$ .

The stochastic time-dependent Ginsburg-Landau equation is used for the time-evolution of the SO parameters  $\eta_p$ :

$$\frac{d\eta_p(\mathbf{r}, t)}{dt} = -M \frac{\delta F}{\delta \eta_p(\mathbf{r}, t)} + \zeta_p(\mathbf{r}, t), \quad p = 1 - 12, \quad (10)$$

where  $t$  is time,  $\zeta$  is the Langevin noise term describing thermal fluctuations [37,38], and  $M$  is the kinetic coefficient characterizing the growth of martensitic domains. The homogeneous modulus assumption [10] (i.e., the elastic modulus remains unchanged in B2 and B19' phases) is made, and the length scale of the simulation is determined as  $l_0 = 1$  nm. The simulation supercell is  $64^3 \text{ nm}^3$  with a periodical boundary condition along all three dimensions. The local stress field is constituted with  $4 \times 4 \times 4$  continuum stress field  $\mathbf{\Pi}(\mathbf{r})$  from 64 individual MD simulations (box size is  $16^3 \text{ nm}^3$ ) with different random seeds.

### III. RESULTS AND DISCUSSION

Four random processes of introducing PKAs with different energies (i.e., different velocities in MD simulation) into a perfect B2 NiTi structure are implemented, and the densities of the interstitial and antisite atoms are shown in Figs. 2(a) and 2(b). The fluence describes the quantity of the high-energy particles impacting the sample during irradiation, and its unit is always  $\text{cm}^{-2}$ , which means the density of particles on the surface. Different from experiments, we use the PKAs

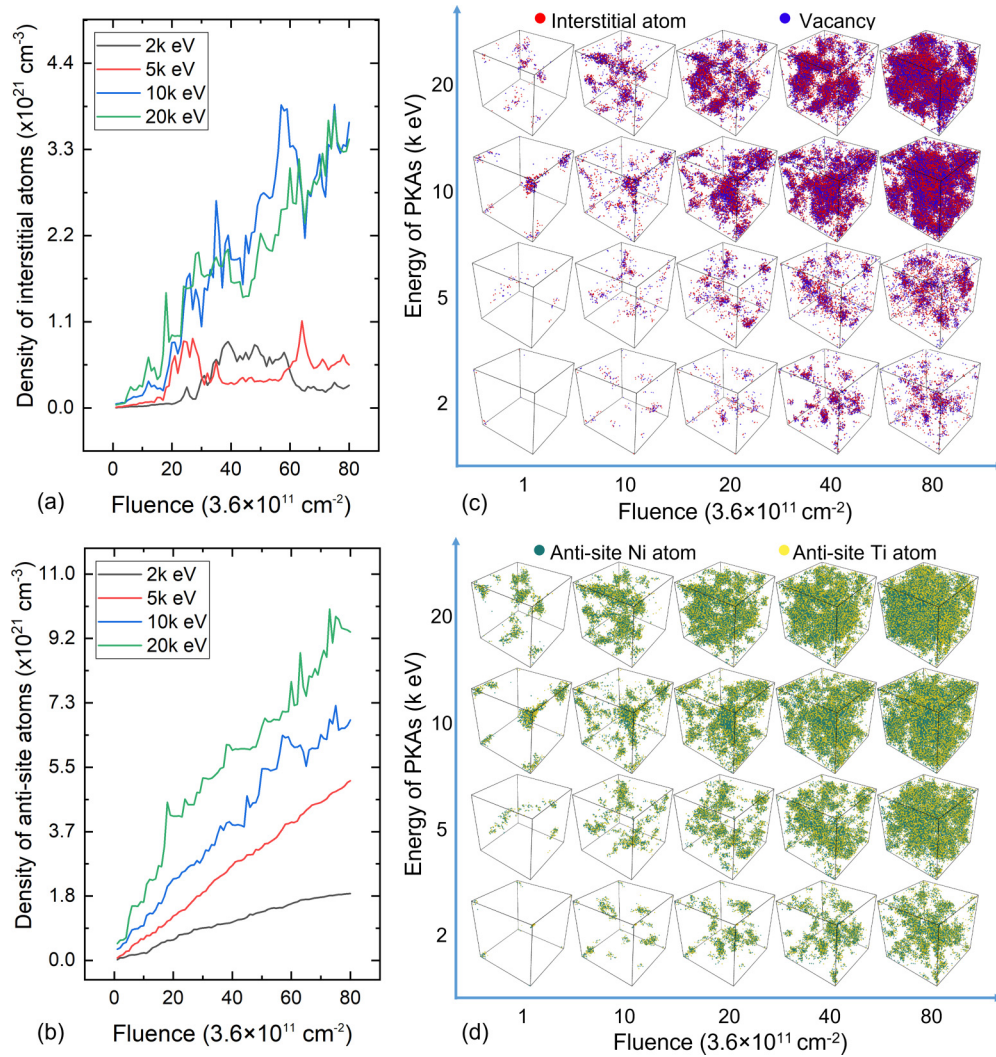


FIG. 2. (a) and (b) The density of the interstitial atom and the antisite atom vs the irradiation fluence for different energies (2, 5, 10, and 20 keV) of the primary knock-on atom (PKA). (c) and (d) The distribution of point defects after the irradiation with different fluences and energies. The red and blue spheres in (c) indicate the interstitial atoms and vacancies, while the green and yellow spheres in (d) indicate the antisite Ni and Ti atoms, and the transparent area represents the B2 structure.

instead of high-energy particles to describe the fluence in MD simulations, which assume a high-energy particle may induce one PKA. The fluence is discrete with a unit fluence  $f_0$  [ $1/(55a_0 \times 55a_0) \sim 3.6 \times 10^{11} \text{ cm}^{-2}$ ], which is one PKA in the box of  $55a_0 \times 55a_0 \times 55a_0$  because of the integer number of PKAs. It is readily seen in Fig. 2(a) that, for the process with low PKA energy (2–5 keV), the density of the interstitial atoms slowly increases firstly, then sharply increases, and fluctuates finally with the further increase of irradiation fluence. For the process with high PKA energy (10–20 keV), the curves show a near-linear increase with weak fluctuation. The related microstructure in Fig. 2(c) shows that the PKAs only cause isolated clusters of interstitial atoms and vacancies at the beginning of the low-energy processes, and the newly added PKA will interact with the clusters of interstitial atoms and vacancies and create more defects with the increase of fluence. The severe fluctuation of interstitial atoms can be attributed to the annihilation of interstitial atoms and vacancies in the irradiation processes. The annihilation plays the dominating role in the low level of interstitial atom density.

In contrast, for the high PKA energy processes, the increase of defects caused by cascades is more than the decrease of defects caused by annihilation, leading to a steady increase in the density of the interstitial atoms. With the increase of PKA energy from 5 to 10 keV, the density of the interstitial atoms increases obviously, but the density of the interstitial atoms remains unchanged when PKA is  $>10$  keV. However, the number of antisite defects shows a near-linear increase with smaller fluctuations with the increase of irradiation fluence for all PKA energy processes, as shown in Fig. 2(b), which can be attributed to the more stable energy condition of the antisite atoms than that of interstitial atoms. The density of the antisite atoms also increases with PKA energy from 2 to 20 keV. The formation energies of different types of point defects are listed in Table I. For the interstitial atom, there are four types of positions, i.e., (1) octahedron with 4 Ni atoms and 2 Ti atoms, (2) octahedron with 4 Ti atoms and 2 Ni atoms, (3) self-dumbbell with the same kind of atom at one lattice point, and (4) pair-dumbbell with the other kind of atom at one lattice point. It is readily seen that the self-dumbbell position,

TABLE I. Formation energy (eV) of different point defects.

Element	Vacancy	Antisite	Interstitial		Self-dumbbell	Pair-dumbbell
			(4Ni2Ti)	(4Ti2Ni)		
Ni	5.89	0.99	15.23	17.01	6	7.46
Ti	6.53	1.94	26.16	20.91	12.64	14.35

which is the self-interstitial atom (SIA), has the lowest energy for both Ni and Ti, and it has slightly larger energy than the vacancy and much larger energy than the antisite atom.

The distribution of the interstitial atoms and vacancies identified with the Weigner-Seitz cell method after different irradiation fluences with different energies of the PKA is shown in Fig. 2(c), in which the red particles, blue particles, and transparent area indicate the interstitial atoms, vacancies, and the B2/body-centered cubic structure, respectively. It is clearly shown that there are isolated defects at low irradiation fluence but clusters of interstitial atoms and vacancies (2–10 nm) at high irradiation fluence. Figure 2(d) shows the distribution of antisite Ni and Ti atoms indicated with green and yellow particles. There is also a similar phenomenon shown in Fig. 2(c) of the isolated clusters at low irradiation fluence and larger clusters (2–10 nm) when increasing the irradiation fluence. In addition, it is also distinct that the antisite atoms appear accompanied by the interstitial atoms and vacancies at low irradiation fluence, and the antisite atoms show a much larger cluster and density, especially at 5 keV and 80  $f_0$  at high irradiation fluence due to the annihilation of the interstitial atoms and vacancies.

Although the nucleation of a void during irradiation may lead to failure and deterioration of the SE, experimental works have shown no voids observed in NiTi alloys after low irradiation level (e.g., 2 MeV and  $10^{15}$  cm<sup>-2</sup> proton irradiated Ni<sub>50.5</sub>Ti<sub>49.5</sub> [39], 3 MeV and  $5 \times 10^{16}$  cm<sup>-2</sup> proton irradiated Ni<sub>50</sub>Ti<sub>50</sub> [40], and 18 MeV and  $1.5 \times 10^{14}$  cm<sup>-2</sup> proton irradiated Ni<sub>50.6</sub>Ti<sub>49.4</sub> [24]). The PKA energy and fluence used in our calculations are <20 keV and  $2.9 \times 10^{13}$  cm<sup>-2</sup>, which are much smaller than the irradiation levels in the above-mentioned experiments. The atomic structure analysis of the MD results after irradiation has shown no void. According to

the method of Yang *et al.* [41], the simulation box has been divided into many small unit cells with an edge length of 1.01 times the lattice constant, and the empty cells can be recognized as voids. Figure 3(a) shows an example of the atomic configuration after irradiation with 20 keV and 80  $f_0$  has shown the existence of interstitial atoms and vacancies. A corresponding slice across the clusters of interstitial atoms and vacancies is shown in Fig. 3(b), with the thickness of 1.01 times the lattice constant. The number of atoms in every unit cell is counted, and the results are shown in Fig. 3(c). No empty cell (the number value = 0) indicating no void can be observed, but a unit cell with a vacancy (the number value = 1) and interstitial atom (the number value  $\geq 3$ ) can be observed. Thus, it is reasonable to study the MT/STGT without considering the void under low-energy and low-fluence irradiation in this paper.

Figures 4(a)–4(f) show the atomic Von Mises stress field [which is calculated according to Eq. (1)] in the (1 1 0) plane caused by a single antisite Ni atom, a vacancy at the Ni site, a Ni SIA, an antisite Ti atom, a vacancy at the Ti site, and a Ti SIA, respectively, and the defect positions are indicated by the red circles. The small and large spheres in Figs. 4(a)–4(f) represent Ni and Ti atoms, and the color indicates the stress value on the atoms. It is readily seen that the SIA has a much larger stress value than the vacancy and the antisite atom, so the interstitial defect may have a larger influence on MT. The atomic stress only exists at the positions of atoms and shows a discrete value. To introduce the atomic stress to the following phase field simulations, a continuum stress field can be calculated based on Eqs. (2)–(4) [11,32]. The Gaussian localization function in Eq. (3) is used to transfer the stress value on every atom to the whole space and make the discrete stress field into a continuum. The stoichiometric function [Eq. (4)] is implemented to increase the resolution and guarantee the correct proportion of different atoms [32]. To obtain the atomic stress field, we take the atomic configurations directly from the MD simulations in Fig. 2, which contains all the defects formed in the irradiation processes. Figures 4(g)–4(i) show the continuum von Mises stress field (with the box size of 16<sup>3</sup> nm<sup>3</sup>) calculated from the atomic configuration after different irradiation fluences of 1, 10, and 40 with the PKA energy being 20 keV. It is distinct that there

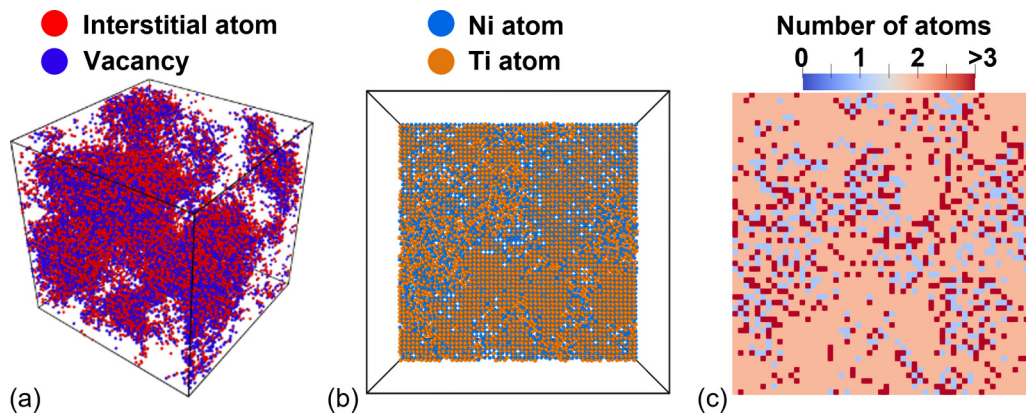


FIG. 3. (a) The distribution of interstitial atoms and vacancies after 20 keV, 80 primary knock-on atoms (PKAs). (b) A slice of the atomic configuration of (a) with the thickness 1.01 times the lattice constant. (c) The corresponding number of atoms in the unit cells of (b).

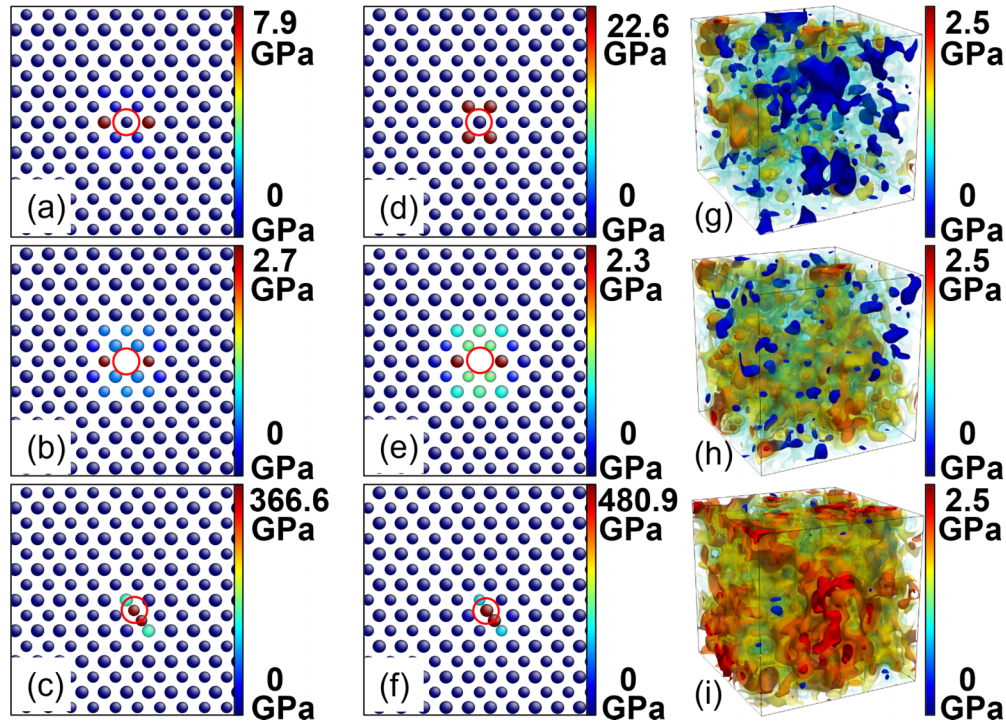


FIG. 4. The calculated atomic stress field caused by a single point defect and the continuum stress field are calculated from the atomic configuration after a certain number of cascades. The color represents the stress value indicated in the corresponding color bar. (a)–(f) The Von Mises stress on atoms caused by a single antisite atom, vacancy, and a self-interstitial atom (SIA) at Ni and Ti sites. The bigger and smaller spheres represent Ti and Ni atoms. (g)–(i) The continuum Von Mises stress field calculated from the atomic configuration after different irradiation fluences ( $1, 10,$  and  $40 \times 3.6 \times 10^{11} \text{ cm}^{-2}$ ) with the energy of the primary knock-on atom (PKA) being 20 keV.

is only a small region colored with a high stress value when the fluence is  $1 f_0$ , and there are several larger domains with a high stress value with the fluence of  $10 f_0$ . However, when the fluence reaches  $40 f_0$ , the whole simulation box is affected by the defects and shows a high stress value. The MT in the region with different stress values needs different driving forces, so the system shows a continuous transition behavior, i.e., STGT.

Figure 5 shows the related martensitic phase transition behavior after irradiation with the same PKA energy of 20 keV and different fluences. The solid curves in Figs. 5(a)–5(p) (first row) show the volume fraction of the martensitic phase during cooling and heating processes after irradiation, while the dash curves show the related heat capacity. The thermal hysteresis ( $\Delta T$ ) is calculated from the difference between the peaks of heat capacity upon cooling and heating and is indicated with arrows. It is readily seen that the MT changes from a sharp first-order transition to a continuum transition, i.e., STGT [7], with the irradiation fluence increasing. The hysteresis decreases with the fluence increasing and achieves nonhysteresis at  $40 f_0$ . The retained austenite also increases from 0 to  $\sim 37\%$  with the fluence increasing, which means that the existence of high-density defects and an amorphous phase which possess a high stress level suppressed the MT. Figures 5(b)–5(q) (second row) show the storage modulus in which the appearance of the frequency dispersion and glass transition temperature  $T_g$  indicate that the systems change from normal MT to STGT with the fluence increasing. The STGT appears at  $20 f_0$ , and the normal MT disappears at  $30 f_0$ . The range of  $20$ – $30 f_0$  is

the crossover range where there is a spontaneous transition from short-range ordered strain glass to long-range ordered martensite [42,43]. Figures 5(c)–5(r) (third row) show the two-dimensional section of the martensitic microstructure at 0 K. It is readily seen that the martensitic domains get smaller and lose the twinning structure with the fluence increasing and finally become nanoscaled domains, which indicate strain glass. Figure 6 shows the phase diagram summarized from the calculations shown in Figs. 5(a)–5(r). The phase diagram is divided into three phases, i.e. austenite, martensite, and strain glass, and the phase boundary between martensite and strain glass is tilted, indicating the spontaneous transition from martensite to strain glass. The MT temperature ( $M_s$ ) and the strain glass temperature ( $T_g$ ) decrease with the fluence increasing.

The statistical analysis of MT and STGT for PKA energy vs irradiation fluence is drawn based on the above calculations, as shown in Fig. 7. In Fig. 7(a), the data points show the type of phase transition, the purple chain curve indicates the boundary between MT and STGT, and the green chain curve indicates the critical irradiation level of nonhysteresis STGT. It is apparent that the transition changes from MT to STGT with the increase of the irradiation fluence and PKA energy. Figure 7(b) shows the linear boundary between the irradiation fluence and the reciprocal of the energy of the PKAs ( $1/E_{\text{PKA}}$ ) according to the points in Fig. 7(a). Our analysis shows that the two critical transition boundaries need constant irradiation energy  $f_{\text{irrad}}$  level with the relationship  $f_{\text{irrad}} = \phi E_{\text{PKA}}$  in the system. In addition, the  $f_{\text{irrad}}$  is calculated as  $\sim 5.9 \times 10^{13} \text{ keV/cm}^2$  and  $\sim 2.2 \times 10^{14} \text{ keV/cm}^2$

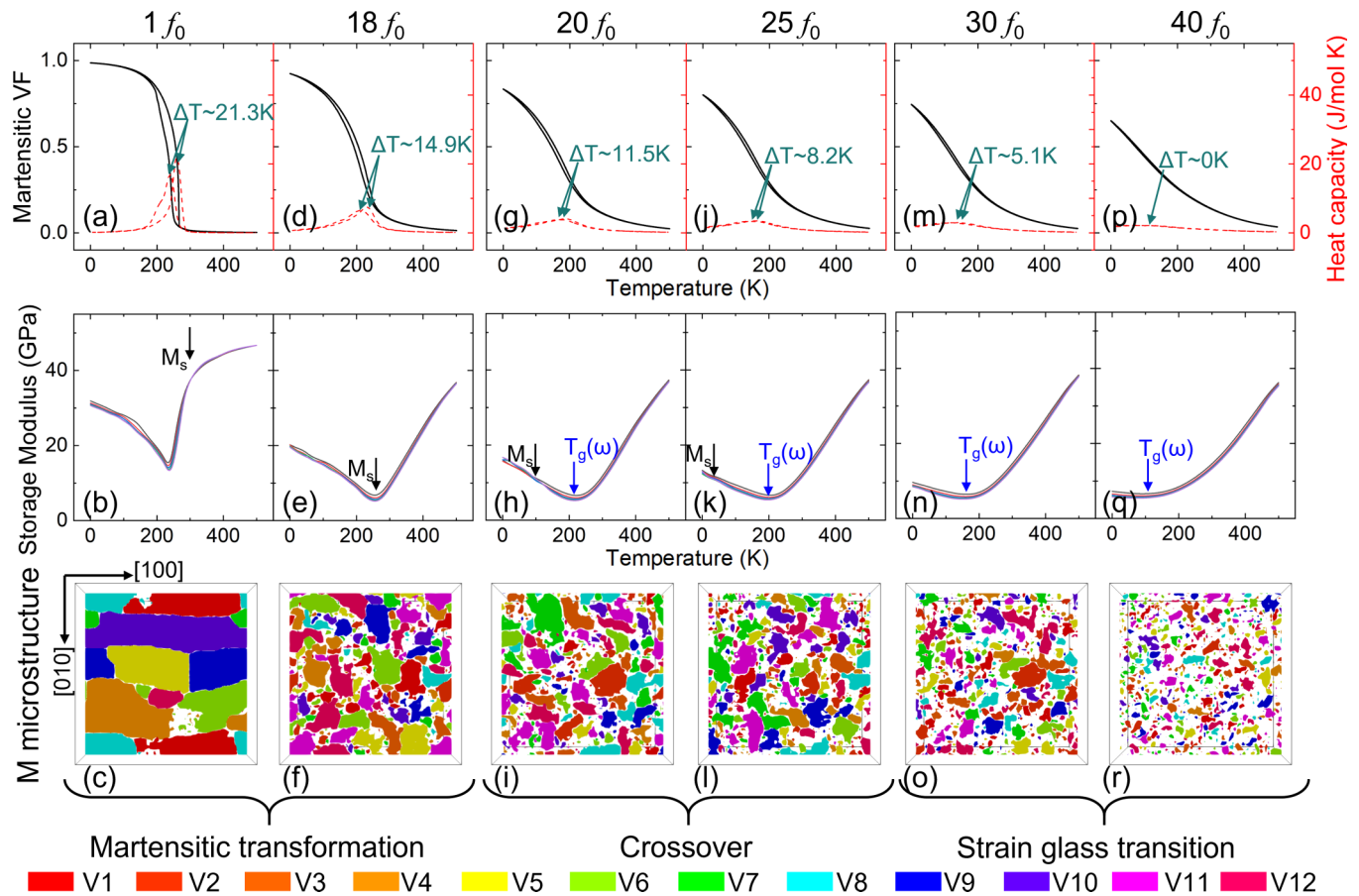


FIG. 5. Phase field modeling results with different fluences of 20 keV primary knock-on atoms (PKAs). (a)–(p) The first row shows the martensitic volume fraction and the heat capacity during cooling and heating. (b)–(q) The second row shows the calculated dynamic mechanical analysis (DMA) results. The third row shows the two-dimensional slices of microstructure at 0 K in which different colors represent different martensitic variants, and the transparent region indicates the parent phase.

for STGT and nonhysteresis STGT, respectively. This result and the constant irradiation energy density provide a guide for designing SMAs with wide-temperature-range SE and small hysteresis by low-energy irradiation.

Figure 8(a) shows the calculated strain-stress curves during the tensile test with applied stress along the [1 1 0] direction at different temperatures (from 100 to 300 K) in systems with different fluences of 20 keV PKAs. It is readily seen that all systems show clear SE at 300 K (above  $A_f$ ), and the hysteresis between the loading and unloading processes decreases with the increase of irradiation fluence. The system with  $\phi = 40 f_0$  shows a total quasilinear elastic response. When the temperature decreases to 200 K, the systems with the irradiation fluence  $\phi = 1$  and  $10 f_0$  show a SME (irrecoverable strain after unloading), while the systems with the irradiation fluence  $\phi = 20$  and  $40 f_0$  still show a SE with small hysteresis (even zero for the system with  $\phi = 40 f_0$ ). At lower temperature  $T = 100$  K, the systems with  $\phi = 1, 10,$  and  $20 f_0$  show a SME (irrecoverable strain after unloading), while the system with  $\phi = 40 f_0$  still shows nonlinear SE with small hysteresis. It is reasonable that the system with  $\phi = 20 f_0$  shows SME instead of SE at 100 K because there is a spontaneous transition from strain glass to martensite at  $\sim 125$  K, as shown in Fig. 6, below which the system is long-range ordered martensite rather than nanoscaled martensitic domains (i.e.,

strain glass). The recoverable strain vs temperature in the systems is shown in Fig. 8(b). It is reported that the recoverable strain decreases with the increase of irradiation fluence at 300 K, while the temperature range for SE increases with the increase of irradiation fluence. Although the recoverable strain in the system with the irradiation fluence  $\phi = 40 f_0$  is smaller than that in the system with the irradiation fluence  $\phi = 1 f_0$  at 300 K, the system with the irradiation fluence  $\phi = 40 f_0$  shows a nonhysteresis SE over a wide temperature range ( $\sim 200$  K). Note that we did not consider the plasticity caused by dislocation slip in our simulations; thus, the elastic strain contributes to  $\sim 2\%$  in our applied stress level (1.2 GPa). Figures 8(c) and 8(d) show the related microstructure evolution for s-s curves of  $\phi = 1$  and  $\phi = 40 f_0$  at 300 K, which explain the origin of the SE with large hysteresis and zero hysteresis. Figure 8(c) shows that the growth of the nanoscaled martensitic domains preferred by the external load (labeled as purple, green, orange, and cyan) also contributes to the linear part at the beginning of the s-s curves upon loading. With the increase of external load, the multivariant nanoscaled martensitic domains grow to long-range ordered martensite with only two variants (purple and cyan) after the stress plateau. The formation of first-ordered and long-range ordered martensite possesses large hysteresis. For the system with  $\phi = 40 f_0$ , Fig. 8(d) shows growth of the external load

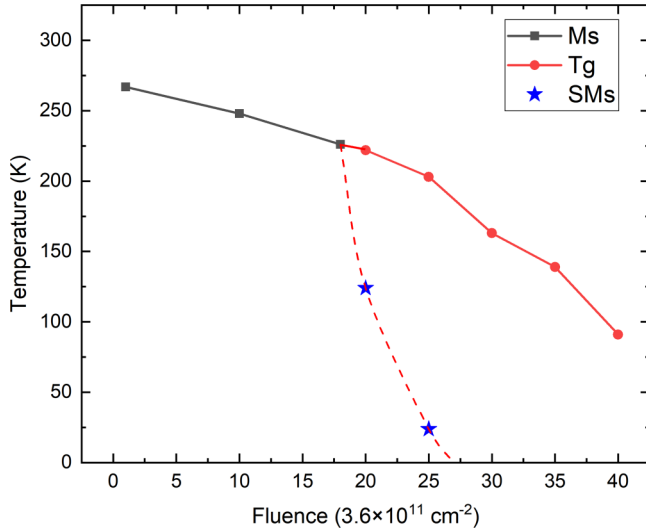


FIG. 6. Martensitic transformation temperature ( $M_s$ ), strain glass transition temperature ( $T_g$ ), and spontaneous transition temperature ( $SM_s$ ) vs irradiation fluence of 20 keV primary knock-on atom (PKA).

preferred the nano martensitic domains (purple and cyan) upon loading, but no long-range ordered martensite appears and no hysteresis. It is notable that there still exist retained austenite and unfavored nano martensitic domains (red, green, orange, blue, etc.) stabilized by the local stress-strain field caused by the defects [11], which are the origin of the smaller SE strain than that in the system with  $\phi = 1 f_0$ .

Although irradiation-induced embrittlement occurs in high-fluence irradiation by eliminating dislocation-mediated plasticity, the MT and STGT in NiTi SMAs could provide an extra deformation mechanism, i.e., phase transition induced plasticity. The deformation mechanisms of the strain glass system can be attributed to the limited nucleation space and growth of the MT in the nanoscale, leading to SE with large recoverable strain and small hysteresis [11].

#### IV. CONCLUSIONS

In summary, a simulation work is proposed to investigate the effect of irradiation on MT by integrating MD, molecular statics with localization, and phase field modeling. MD simulations show the existence of interstitial atoms, vacancies, antisite atoms after irradiation, and the defect density increases with the increase of PKA energy and fluence. The interstitial-vacancy defect pair density could reach  $3.8 \times 10^{21} \text{ cm}^{-3}$  when the irradiation fluence is  $80 \times 3.6 \times 10^{11} \text{ cm}^{-2}$  and the PKA energy is 20 keV. Further calculation of local stress caused by different defects has shown that the interstitial atom could induce the largest misfit, i.e.,  $\sim 15$  times larger than that of the antisite defect and  $\sim 135$  times larger than that of the vacancy. The phase field modeling considering the local stress distribution caused by irradiation defects shows STGT instead of normal MT when the irradiation fluence and the energy of PKA reach the critical value ( $f_{\text{irrad}} = \phi E_{\text{PKA}} = 5.9 \times 10^{13} \text{ keV/cm}^2$ ). The system with high irra-

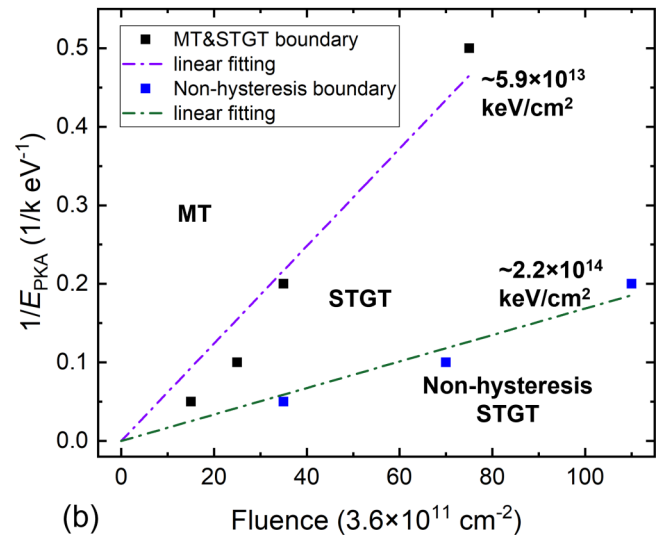
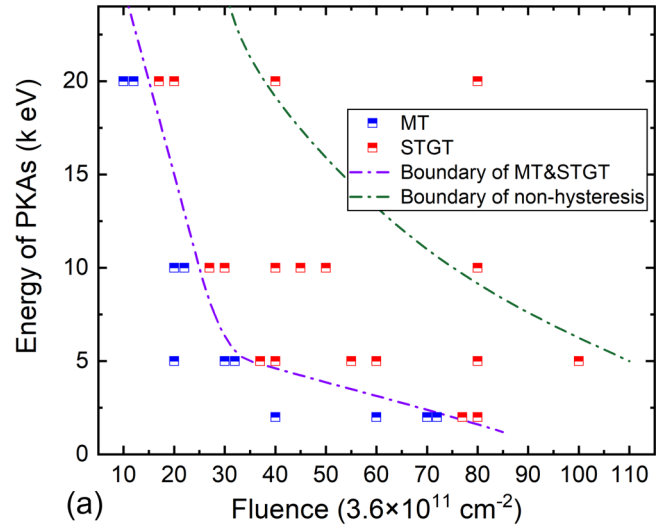


FIG. 7. (a) The phase transition diagram of martensitic transformation (MT) and strain glass transition (STGT) for different energies of the primary knock-on atoms (PKAs) and different irradiation fluences. The purple chain line indicates the boundary between MT and STGT. The green chain line indicates the boundary of nonhysteresis transition. (b) The linear fitting of the irradiation fluence and the reciprocal of the energy of the PKAs at the two boundaries in (a).

diation level has shown SE ( $\sim 5.8\%$ ) with slim hysteresis over a wide temperature range (100–300 K). Moreover, a phase transition diagram for different irradiation fluences and energies of PKA is drawn in which two critical transition behavior boundaries (MT with STGT and nonhysteresis STGT) are indicated with the linear relationship  $f_{\text{irrad}} = \phi E_{\text{PKA}}$ . This paper may serve as a guide to design SMAs with wide-temperature-range SE and small hysteresis by low-energy irradiation.

#### ACKNOWLEDGMENTS

C.L. and D.W. would like to acknowledge support from the National Natural Science Foundation of China (Grants No.

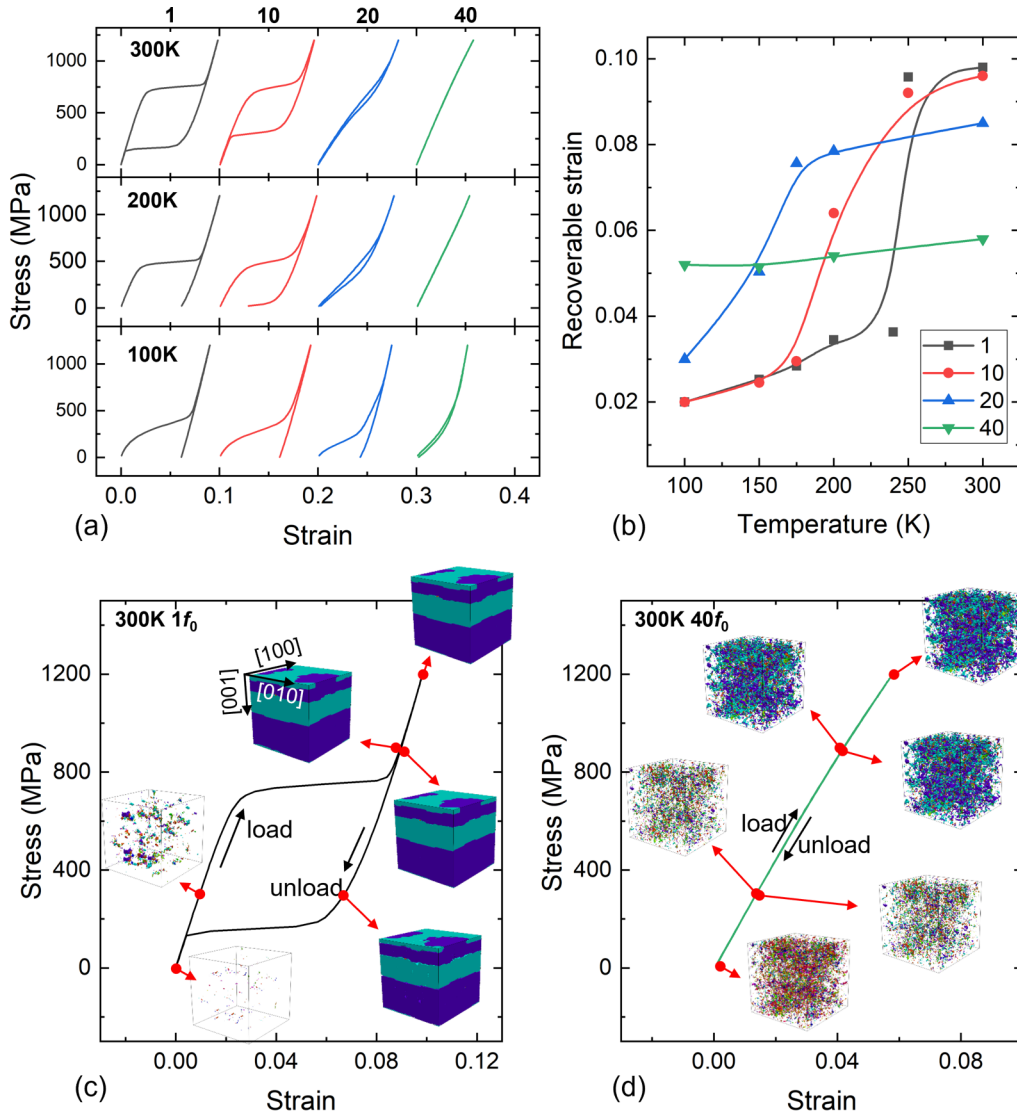


FIG. 8. (a) The calculated stress vs strain curves in systems with different irradiation fluences (1–40 $f_0$ ) of 20 keV primary knock-on atoms (PKAs) at 100–300 K. (b) The corresponding recoverable strain vs temperature in the systems shown in (a). (c) and (d) The microstructure evolution during loading and unloading in systems with 1  $f_0$  and 40  $f_0$  at 300 K.

51931004 and No. 52171012). H.G. would like to acknowledge the National Key Research and Development Program of China (Grant No. 2017YFB0702401), W.L. would like to acknowledge the support from the NSAF Joint Fund (Grants No. U1830124 and No. U2130105)

**APPENDIX: CALCULATION OF THE SFTS TENSORS FROM B2 TO B19'**

The MT can be described as a deformation and formulated by  $\mathbf{e}_i^M = \mathbf{U}\mathbf{e}_i^A$  ( $i = 1, 2, 3$ ), where  $\mathbf{e}^M$  and  $\mathbf{e}^A$  are the lattice vector of martensite and austenite, respectively, and  $\mathbf{U}$  is the transformation matrix. The 12 lattice correspondences between austenite (B2) and martensite (B19') are shown in Table II [44], and the 12 transformation matrixes

are [33]

$$\begin{aligned} \mathbf{U}^1 &= \begin{pmatrix} \gamma & \lambda & \lambda \\ \lambda & \psi & \delta \\ \lambda & \delta & \psi \end{pmatrix}, & \mathbf{U}^2 &= \begin{pmatrix} \gamma & -\lambda & -\lambda \\ -\lambda & \psi & \delta \\ -\lambda & \delta & \psi \end{pmatrix}, \\ \mathbf{U}^3 &= \begin{pmatrix} \gamma & -\lambda & -\lambda \\ -\lambda & \psi & -\delta \\ \lambda & -\delta & \psi \end{pmatrix}, & \mathbf{U}^4 &= \begin{pmatrix} \gamma & \lambda & -\lambda \\ \lambda & \psi & -\delta \\ -\lambda & -\delta & \psi \end{pmatrix}, \\ \mathbf{U}^5 &= \begin{pmatrix} \psi & \lambda & \delta \\ \lambda & \gamma & \lambda \\ \delta & \lambda & \psi \end{pmatrix}, & \mathbf{U}^6 &= \begin{pmatrix} \psi & -\lambda & \delta \\ -\lambda & \gamma & -\lambda \\ \delta & -\lambda & \psi \end{pmatrix}, \\ \mathbf{U}^7 &= \begin{pmatrix} \psi & -\lambda & -\delta \\ -\lambda & \gamma & \lambda \\ -\delta & \lambda & \psi \end{pmatrix}, & \mathbf{U}^8 &= \begin{pmatrix} \psi & \lambda & -\delta \\ \lambda & \gamma & -\lambda \\ -\delta & -\lambda & \psi \end{pmatrix}, \end{aligned}$$

TABLE II. Lattice correspondences between austenite (B2) and martensite (B19') [44].

Variants	[100] <sub>B19'</sub>	[010] <sub>B19'</sub>	[001] <sub>B19'</sub>
1	[100] <sub>B2</sub>	[011] <sub>B2</sub>	[0 $\bar{1}$ 1] <sub>B2</sub>
2	[ $\bar{1}$ 00] <sub>B2</sub>	[0 $\bar{1}\bar{1}$ ] <sub>B2</sub>	[011] <sub>B2</sub>
3	[100] <sub>B2</sub>	[0 $\bar{1}$ 1] <sub>B2</sub>	[0 $\bar{1}\bar{1}$ ] <sub>B2</sub>
4	[ $\bar{1}$ 00] <sub>B2</sub>	[01 $\bar{1}$ ] <sub>B2</sub>	[0 $\bar{1}\bar{1}$ ] <sub>B2</sub>
5	[010] <sub>B2</sub>	[101] <sub>B2</sub>	[10 $\bar{1}$ ] <sub>B2</sub>
6	[0 $\bar{1}$ 0] <sub>B2</sub>	[ $\bar{1}$ 0 $\bar{1}$ ] <sub>B2</sub>	[10 $\bar{1}$ ] <sub>B2</sub>
7	[010] <sub>B2</sub>	[10 $\bar{1}$ ] <sub>B2</sub>	[ $\bar{1}$ 0 $\bar{1}$ ] <sub>B2</sub>
8	[0 $\bar{1}$ 0] <sub>B2</sub>	[ $\bar{1}$ 01] <sub>B2</sub>	[ $\bar{1}$ 0 $\bar{1}$ ] <sub>B2</sub>
9	[001] <sub>B2</sub>	[110] <sub>B2</sub>	[ $\bar{1}$ 10] <sub>B2</sub>
10	[00 $\bar{1}$ ] <sub>B2</sub>	[ $\bar{1}\bar{1}$ 0] <sub>B2</sub>	[ $\bar{1}$ 10] <sub>B2</sub>
11	[001] <sub>B2</sub>	[ $\bar{1}$ 10] <sub>B2</sub>	[ $\bar{1}\bar{1}$ 0] <sub>B2</sub>
12	[00 $\bar{1}$ ] <sub>B2</sub>	[1 $\bar{1}$ 0] <sub>B2</sub>	[ $\bar{1}\bar{1}$ 0] <sub>B2</sub>

$$\mathbf{U}^9 = \begin{pmatrix} \psi & \delta & \lambda \\ \delta & \psi & \lambda \\ \lambda & \lambda & \gamma \end{pmatrix}, \quad \mathbf{U}^{10} = \begin{pmatrix} \psi & \delta & -\lambda \\ \delta & \psi & -\lambda \\ -\lambda & -\lambda & \gamma \end{pmatrix},$$

$$\mathbf{U}^{11} = \begin{pmatrix} \psi & -\delta & \lambda \\ -\delta & \psi & -\lambda \\ \lambda & -\lambda & \gamma \end{pmatrix}, \quad \mathbf{U}^{12} = \begin{pmatrix} \psi & -\delta & -\lambda \\ -\delta & \psi & \lambda \\ -\lambda & \lambda & \gamma \end{pmatrix},$$

where  $\psi$ ,  $\gamma$ ,  $\lambda$ , and  $\delta$  depend on lattice parameters. According to Ref. [33],  $\psi = 1.0243$ ,  $\gamma = 0.9563$ ,  $\lambda = -0.0427$ , and  $\delta = 0.058$ . The SFTS tensors from B2 to B19' can be calculated as  $\varepsilon = \frac{\mathbf{U}^T \mathbf{U} - \mathbf{I}}{2}$ , where  $\mathbf{U}^T$  is the transpose of  $\mathbf{U}$ , and  $\mathbf{I}$  is the identity matrix. The calculated SFTS tensors are

$$\varepsilon^1 = \begin{pmatrix} -0.0409 & -0.0435 & -0.0435 \\ -0.0435 & 0.0272 & 0.0603 \\ -0.0435 & 0.0603 & 0.0272 \end{pmatrix},$$

$$\varepsilon^2 = \begin{pmatrix} -0.0409 & 0.0435 & 0.0435 \\ 0.0435 & 0.0272 & 0.0603 \\ 0.0435 & 0.0603 & 0.0272 \end{pmatrix},$$

$$\varepsilon^3 = \begin{pmatrix} -0.0409 & 0.0435 & -0.0435 \\ 0.0435 & 0.0272 & -0.0603 \\ -0.0435 & -0.0603 & 0.0272 \end{pmatrix},$$

$$\varepsilon^4 = \begin{pmatrix} -0.0409 & -0.0435 & 0.0435 \\ -0.0435 & 0.0272 & -0.0603 \\ 0.0435 & -0.0603 & 0.0272 \end{pmatrix},$$

$$\varepsilon^5 = \begin{pmatrix} 0.0272 & -0.0435 & 0.0603 \\ -0.0435 & -0.0409 & -0.0435 \\ 0.0603 & -0.0435 & 0.0272 \end{pmatrix},$$

$$\varepsilon^6 = \begin{pmatrix} 0.0272 & 0.0435 & 0.0603 \\ 0.0435 & -0.0409 & 0.0435 \\ 0.0603 & 0.0435 & 0.0272 \end{pmatrix},$$

$$\varepsilon^7 = \begin{pmatrix} 0.0272 & 0.0435 & -0.0603 \\ 0.0435 & -0.0409 & -0.0435 \\ -0.0603 & -0.0435 & 0.0272 \end{pmatrix},$$

$$\varepsilon^8 = \begin{pmatrix} 0.0272 & -0.0435 & -0.0603 \\ -0.0435 & -0.0409 & 0.0435 \\ -0.0603 & 0.0435 & 0.0272 \end{pmatrix},$$

$$\varepsilon^9 = \begin{pmatrix} 0.0272 & 0.0603 & -0.0435 \\ 0.0603 & 0.0272 & -0.0435 \\ -0.0435 & -0.0435 & -0.0409 \end{pmatrix},$$

$$\varepsilon^{10} = \begin{pmatrix} 0.0272 & 0.0603 & 0.0435 \\ 0.0603 & 0.0272 & 0.0435 \\ 0.0435 & 0.0435 & -0.0409 \end{pmatrix},$$

$$\varepsilon^{11} = \begin{pmatrix} 0.0272 & -0.0603 & 0.0435 \\ -0.0603 & 0.0272 & 0.0435 \\ -0.0435 & 0.0435 & -0.0409 \end{pmatrix},$$

$$\varepsilon^{12} = \begin{pmatrix} 0.0272 & -0.0603 & 0.0435 \\ -0.0603 & 0.0272 & -0.0435 \\ 0.0435 & -0.0435 & -0.0409 \end{pmatrix}.$$

- [1] K. Otsuka and X. Ren, *Prog. Mater. Sci.* **50**, 511 (2005).  
[2] M. Elahinia, N. S. Moghaddam, M. T. Andani, A. Amerinatanzi, B. A. Bimber, and R. F. Hamilton, *Prog. Mater. Sci.* **83**, 630 (2016).  
[3] A. T. Clare, P. R. Chalker, S. Davies, C. J. Sutcliffe, and S. Tsoupanos, *Int. J. Mech. Mater. Des.* **4**, 181 (2007).  
[4] S. Miyazaki, Y. Ohmi, K. Otsuka, and Y. Suzuki, *J. Phys.* **43**, C4-255 (1982).  
[5] F. Xiao, T. Fukuda, and T. Kakeshita, *Philos. Mag.* **95**, 1390 (2015).  
[6] A. Kosogor, V. A. L'vov, V. A. Chernenko, E. Villa, J. M. Barandiaran, T. Fukuda, T. Terai, and T. Kakeshita, *Acta Mater.* **66**, 79 (2014).  
[7] S. Sarkar, X. Ren, and K. Otsuka, *Phys. Rev. Lett.* **95**, 205702 (2005).  
[8] Y. Zhou, D. Xue, X. Ding, Y. Wang, J. Zhang, Z. Zhang, D. Wang, K. Otsuka, J. Sun, and X. Ren, *Acta Mater.* **58**, 5433 (2010).  
[9] Y. Zhou, D. Xue, Y. Tian, X. Ding, S. Guo, K. Otsuka, J. Sun, and X. Ren, *Phys. Rev. Lett.* **112**, 025701 (2014).  
[10] D. Wang, S. Hou, Y. Wang, X. Ding, S. Ren, X. Ren, and Y. Wang, *Acta Mater.* **66**, 349 (2014).  
[11] C. X. Liang, D. Wang, Z. Wang, X. D. Ding, and Y. Z. Wang, *Acta Mater.* **194**, 134 (2020).  
[12] Q. L. Liang, D. Wang, J. Zhang, Y. C. Ji, X. D. Ding, Y. Wang, X. B. Ren, and Y. Z. Wang, *Phys. Rev. Materials* **1**, 033608 (2017).  
[13] Y. Ji, X. Ding, T. Lookman, K. Otsuka, and X. Ren, *Phys. Rev. B* **87**, 104110 (2013).

- [14] D. Wang, Z. Zhang, J. Zhang, Y. M. Zhou, Y. Wang, X. D. Ding, Y. Z. Wang, and X. B. Ren, *Acta Mater.* **58**, 6206 (2010).
- [15] J. Cui and X. B. Ren, *Appl. Phys. Lett.* **105**, 061904 (2014).
- [16] D. Wang, D. Lv, Y. Gao, Y. Wang, X. Ren, and Y. Wang, *J. Alloys Compd.* **661**, 100 (2016).
- [17] W. Schilling, *J. Nucl. Mater.* **69–70**, 465 (1978).
- [18] R. Schmidt, M. Schlereth, H. Wipf, W. Assmus, and M. Mullner, *J. Phys.: Condens. Matter* **1**, 2473 (1989).
- [19] J. Frenzel, Z. Zhang, C. Somsen, K. Neuking, and G. Eggeler, *Acta Mater.* **55**, 1331 (2007).
- [20] I. Sieber, H. Lange, and K. Schade, *Phys. Stat. Sol. (A)* **126**, 171 (1991).
- [21] Y. D. Zhao, R. Ning, X. Y. Yi, Z. Y. Gao, H. Z. Wang, and W. Cai, *Mater. Charact.* **164**, 110348 (2020).
- [22] T. B. Lagrange and R. Gotthard, *J. Optoelectron. Adv. Mater.* **5**, 313 (2003).
- [23] H. Z. Wang, X. Y. Yi, Y. Y. Zhu, Y. K. Yin, Y. Gao, W. Cai, and Z. Y. Gao, *Appl. Surf. Sci.* **419**, 91 (2017).
- [24] Z. G. Wang, X. T. Zu, L. J. Liu, S. Zhu, Y. Huo, L. B. Lin, X. D. Feng, and L. M. Wang, *Nucl. Instrum. Methods Phys. Res. B* **211**, 239 (2003).
- [25] X. Yang, X. G. Zeng, L. Chen, Y. Guo, H. Y. Chen, and F. Wang, *Nucl. Instrum. Methods Phys. Res. B* **436**, 92 (2018).
- [26] M. R. Tonks, A. Cheniour, and L. Aagesen, *Comput. Mater. Sci* **147**, 353 (2018).
- [27] S. Plimpton, *J. Comput. Phys.* **117**, 1 (1995).
- [28] W. S. Lai and B. X. Liu, *J. Phys.: Condens. Matter* **12**, L53 (2000).
- [29] R. Clausius, *London Edinburgh Dublin Philos. Mag. J. Sci.* **40**, 122 (1870).
- [30] J. C. Maxwell, *Trans. R. Soc. Edinburgh* **26**, 1 (1870).
- [31] J. Clerk-Maxwell, *Nature (London)* **10**, 477 (1874).
- [32] P. S. Branicio and D. J. Srolovitz, *J. Comput. Phys.* **228**, 8467 (2009).
- [33] K. Bhattacharya, *Microstructure of Martensite: Why It Forms and How It Gives Rise to the Shape-Memory Effect* (Oxford University Press, Oxford, 2003), Vol. 2.
- [34] J. W. Cahn, *Acta Metall.* **9**, 795 (1961).
- [35] A. G. Khachaturyan and G. A. Shatalov, *Fiz. Tverd. Tela* **11**, 59 (1969) [*Sov. Phys. Solid State* **11**, 118 (1969)].
- [36] A. G. Khachaturyan, *Theory of Structural Transformations in Solids* (Wiley, New York, 1983).
- [37] K. Elder, H. Gould, and J. Tobochnik, *Comput. Phys.* **7**, 27 (1993).
- [38] C. Shen, J. P. Simmons, and Y. Wang, *Acta Mater.* **55**, 1457 (2007).
- [39] N. Afzal, I. M. Ghauri, F. E. Mubarik, and F. Amin, *Physica B* **406**, 8 (2011).
- [40] H. Z. Wang, X. Y. Yi, Y. Y. Zhu, S. B. Sun, Y. Gao, W. Cai, and Z. Y. Gao, *Mater. Charact.* **140**, 122 (2018).
- [41] X. Yang, X. G. Zeng, J. Wang, J. B. Wang, F. Wang, and J. Ding, *Mech. Mater.* **135**, 98 (2019).
- [42] J. Zhang, Y. Wang, X. Ding, Z. Zhang, Y. Zhou, X. Ren, D. Wang, Y. Ji, M. Song, K. Otsuka *et al.*, *Phys. Rev. B* **84**, 214201 (2011).
- [43] Y. Ji, X. Ding, D. Wang, K. Otsuka, and X. Ren, *Phys. Rev. B* **92**, 241114(R) (2015).
- [44] O. Matsumoto, S. Miyazaki, K. Otsuka, and H. Tamura, *Acta Metall.* **35**, 2137 (1987).